frontiers in Materials

ORIGINAL RESEARCH
published: 10 March 2022
doi: 10.3389/fmats.2022.841503

Metal-Organic Framework-Based Nanotherapeutics With Tumor Hypoxia-Relieving Ability for Synergistic Sonodynamic/Chemotherapy

Lichang Zhong[1], *Tian Yang*[2,3,4], *Pei Li*[5], *Lin Shi*[1], *JinYu Lai*[1] *and Liping Gu*[1]*

[1]Department of Medical Ultrasound, Shanghai Jiaotong University Affiliated Sixth People's Hospital, Shanghai, China, [2]The International Peace Maternity and Child Health Hospital, School of Medicine, Shanghai Jiao Tong University, Shanghai, China, [3]Shanghai Key Laboratory of Embryo Original Diseases, Shanghai, China, [4]Shanghai Municipal Key Clinical Specialty, Shanghai, China, [5]Department of Ultrasound, Zhongshan Hospital, Fudan University, Shanghai, China

OPEN ACCESS

Edited by:
Junjie Li,
Innovation Centre of NanoMedicine (iCONM), Japan

Reviewed by:
Dan Shao,
South China University of Technology, China
Panyue Wen,
University of Science and Technology of China, China
Amit Ranjan Maity,
Amity University Kolkata, India

***Correspondence:**
Liping Gu
guliping666@126.com

Specialty section:
This article was submitted to Biomaterials, a section of the journal Frontiers in Materials

Received: 22 December 2021
Accepted: 21 February 2022
Published: 10 March 2022

Citation:
Zhong L, Yang T, Li P, Shi L, Lai J and Gu L (2022) Metal-Organic Framework-Based Nanotherapeutics With Tumor Hypoxia-Relieving Ability for Synergistic Sonodynamic/Chemotherapy. Front. Mater. 9:841503. doi: 10.3389/fmats.2022.841503

Hypoxia, a hallmark of cancer, compromises the efficacy of chemotherapy and other oxygen-dependent modalities (e.g., sonodynamic therapy). For monotherapy, this effect becomes more pronounced because of drug resistance and an adaptive tumor microenvironment. To overcome this, here, we reported metal–organic framework (MOF)-based nanotherapeutics (DOX/Ce6@ZIF-8@PDA) to simultaneously deliver Ce6 and doxorubicin for synergistic sonodynamic/chemotherapy. Notably, O_2 storage ability of MOFs relieves tumor hypoxia to sensitize the tumor to sonodynamic therapy and chemotherapy. Moreover, polydopamine (PDA) promotes endocytosis and enhances intracellular drug concentration. The pH-responsive property of MOFs enables controlled drug release. The *in vitro* and *in vivo* results validate the impressive tumor inhibition, implying the potential of this combination therapy for cancer treatment.

Keywords: sonodynamic therapy, cancer therapy, metal–organic frameworks, hypoxia, drug delivery

1 INTRODUCTION

The mortality rate of cancer has decreased over the past decade as reported by many studies. However, bone tumors are still one of the unsettled diseases in modern medicine threatening human life. Thus, the battle against tumors is continuing in both basic and clinical research (Siegel et al., 2017). To cause damage or death of tumor cells, reactive oxygen species (ROS) have proved to be a reliable mechanism, which have been studied by many research groups. Therefore, as the most widespread components in ROS, O_2 and •OH are effective in hampering tumor cells and damaging the tumor microenvironment. In addition, it has been reported that cancer therapies mediated by ROS can concentrate different redox states and cause more damage to cancer cells than normal cells, which endows them to be competitive in universal cancer treatments (Zhou et al., 2016). In sum, oxygen will also increase the sensitivity of chemotherapy. Among most accepted tumor therapies, Ce6 is expected to provide singlet oxygen ($^1O_2$) with O_2 with an ultrasonic wave; then, the generated $^1O_2$ is able to induce cell apoptosis. Although the generation of $^1O_2$ by Ce6 can effectively reduce the tumor cells, the therapeutic efficiency can be reduced by the tumor microenvironment (TME) with hypoxia significantly (Fan et al., 2016), which limits O_2 in the surrounding microenvironment and hinder $^1O_2$ transformation (Pouysségur et al., 2006; Frésard et al., 2019). Moreover, rapid cell

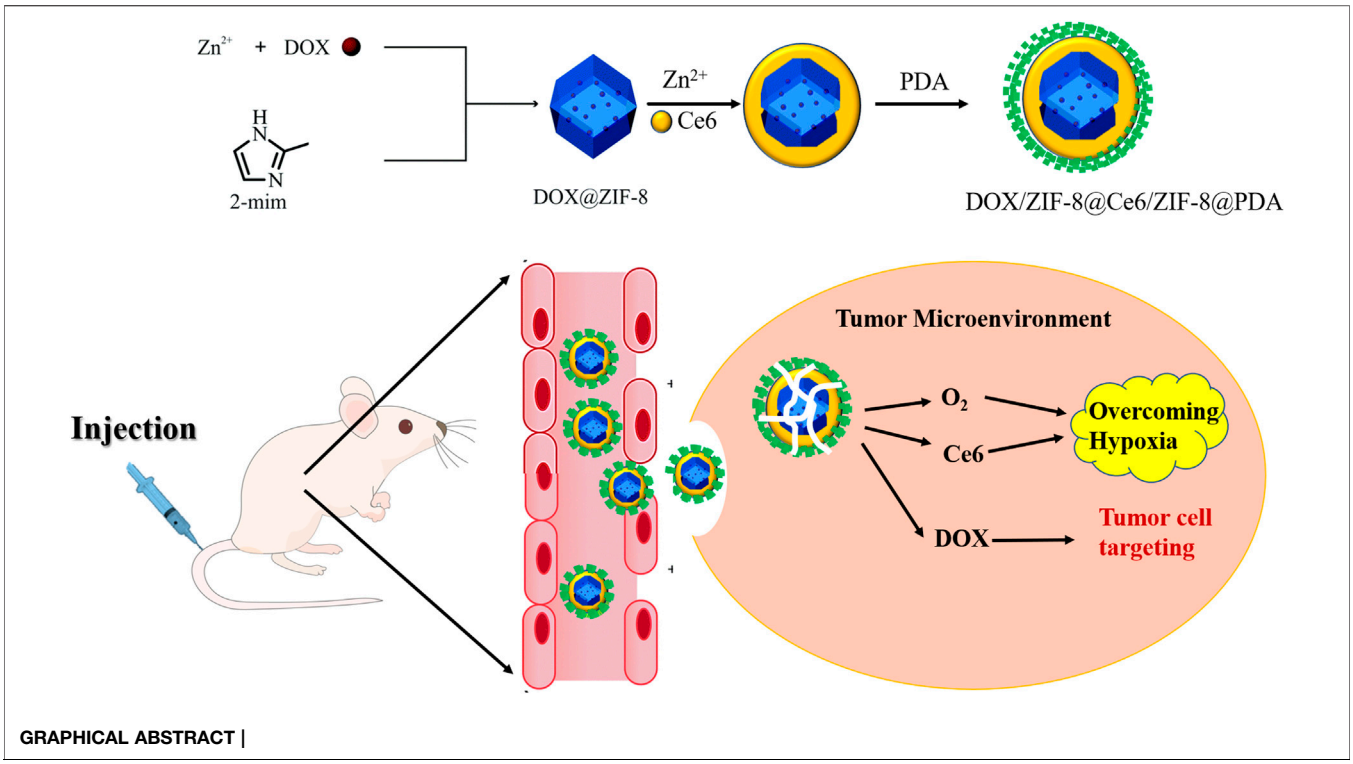

GRAPHICAL ABSTRACT |

proliferation of cancers, in turn, results in a hypoxia condition in most of the tumors and blocks further $^1O_2$ transformation. In such cases, the generation of O_2 in a large amount is warranted in antitumor therapies. To solve this issue, it is reported that O_2 storage materials, such as hemoglobin (Modery-Pawlowski et al., 2013), perfluorocarbon (Cheng et al., 2015), light-triggered clustered vesicles (Li et al., 2017), and metal–organic frameworks (MOFs) (Cai et al., 2019), have been introduced into this area to relieve the hypoxia condition within tumors.

Based on the emergence of multidrug resistance of tumor cells, the use of a single drug often cannot achieve complete remission of cancer. At present, the method of loading a variety of drugs into a nano-carrier for combined treatment can achieve synergistic therapeutic effects (Li and Kataoka, 2021), which attracts extensive attention in the field of tumor research. Meanwhile, drug delivery and its controlled release are highly concentrated. Thus, during the development of tumor therapies, sonodynamic therapy (SDT) has been introduced to the clinics as an accurate controllable method, and doxorubicin (DOX) has begun to be used in burgeoning cancer treatments (Li et al., 2021). As reported, drug resistance of tumors may also be attributed to the complicated TME and indicates the limits of single-drug cancer therapies. Thus, combination therapies are applied to solve this problem for maximizing their efficacy and minimizing the drug doses, with more accurate treatments to the tumor location (Sharma and Allison, 2015; Xie et al., 2019a). Moreover, it is important to explore novel systems that could integrate multiple treatments (Ng et al., 2020; Sun et al., 2021). As a nanoparticle platform, a MOF can be one of such systems to combine multiple treatments and to integrate them for efficacy enhancement (Xie et al., 2019b).

MOFs, one of the highly concentrated porous materials, are an organic–inorganic hybrid, built up by metal ions and organic ligands via coordinate bonds (Ha et al., 2021; Zeng et al., 2021). In the field of oncotherapy, the unique advantages of MOFs, including porosity, species and property diversities, and controllable degradability, indicate its biological friendliness in medical applications and widespread scope (Sheta et al., 2019; Basaleh and Sheta, 2021). In the MOF family, Yaghi's group first reported zeolitic imidazolate frameworks (ZIFs) with exceptional chemical and thermal stabilities (Park et al., 2006; Tao et al., 2021). Due to the excellent thermal and hydrothermal stability, ZIFs have been applied in gas storage, drug carriers, and other biological applications (Banerjee et al., 2008; Wang et al., 2008). Additionally, ZIF-8 has gained attention for its low toxicity under certain conditions (Adhikari et al., 2015) and can be synthesized from zinc ion and 2-methylimidazole (Guo et al., 2020; Choi et al., 2021). In addition, as a stable solvent in a neutral aqueous microenvironment, ZIF-8 can only be decomposed in acidic solutions, indicating its application as a pH-sensitive drug delivery carrier. The high amount of pore cavities in ZIF-8 renders it with perfect drug storage ability with a pore diameter of 11.6 Å but a pore opening of only 3.4 Å (Lu et al., 2009). Therefore, the pore opening is smaller than most anticancer drugs and can prevent premature drug release in physiological conditions. The large pore diameter indicates that the pore cavity can hold a drug until its decomposition under acidic conditions to cancers (Liédana et al., 2012). In

addition, to improve the efficiency of intake of the nanoparticle (NP) by tumor cells, polydiacetylene (PDA) was applied to this nanoparticle on the surface. As a polymer with excellent biocompatibility and degradability, PDA can be synthesized from the reaction of dopamine self-polymerization in a weakly alkaline environment. PDA can also form a conformal layer on NP surfaces (Poinard et al., 2018), which can not only increase the intake efficiency but also help in the ultrasonic treatment controllability by preventing drug leaking *in vivo*. Hence, if we further integrated PDA into nanoparticles, a therapeutic nanoplatform with improved biocompatibility and cell intake efficiency under SDT could be achieved, which could be a potential TME-responsive combination therapy (Lan et al., 2019).

In this study, DOX/Ce6@ZIF-8@PDA (DZCP) core–shell nanostructures were manufactured to destruct tumor hypoxia and cooperate with antitumor cells to enhance SDT. DOX-doped ZIF-8 nanoparticles (DOX/ZIF-8) were synthesized by an ion doping strategy. Then, DOX/ZIF-8 was coated with a thin layer of ZIF-8 capsules, namely, Ce6, and then covered with a PDA layer, to ensure good biocompatibility and cell intake. Therefore, post-intravenous injection (IV), due to the enhanced permeability and retention (EPR) effect, DZCP may accumulate in the tumor site (Shi et al., 2017; Cabral et al., 2018), causing the release of O_2, DOX, and Ce6 within the weakly acidic TME. Thus, a large amount of oxygen can relieve tumor hypoxia and allow Ce6 to quickly produce abundant cytotoxic $^1O_2$ under ultrasound. Therefore, this indicated that nanomedicine shows synergistically improved antitumor efficacy *in vitro* and *in vivo*.

2 MATERIALS AND METHODS

2.1 Materials

Methanol, hydrogen peroxide (H_2O_2, 30%), and zinc nitrate hexahydrate (≥98%) were purchased from Shanghai Aladdin Biochemical Technology Co., Ltd., $Zn(NO_3)_2{\cdot}6H_2O$), 2-methylimidazole (98%, $C_4H_6N_2$, 2-MI), doxorubicin (C27H29NO11, DOX), Ce6, 4,6-diamino-2-phenyl indole (DAPI), and MTT assay, were purchased from Thermo Fisher Co., Ltd.; the hypoxia/oxidative stress detection kit was obtained from Enzo Life Sciences, and the annexin V-FITC/PI double staining apoptosis detection kit was purchased from Beyotime Biotechnology Co., Ltd.

2.2 Characterization Instrument

The scanning electron microscope (SEM) [S-4800 (Hitachi)] was operated at an acceleration voltage of 10 kV with 8 mm working distance. The transmission electron microscope (TEM) was operated at 200 kV with 8 mm working distance. The automatic volumetric adsorption instrument (Micromeritics ASAP 2020; Zhao et al., 2012) was operated at 77 and 298 K for nitrogen and oxygen condition. The Vertex PerkinElmer 580BIR spectrophotometer (Bruker) was used for the FT-IR experiment. The X-ray photoelectron spectroscope used was ESCALAB 250. In the nitrogen stream, the TGA experiment was measured by using a thermal analyzer (SDT 2960, TA Instruments, New Castle, DE). In this study, SDT was set at 1.0 MHz. X-ray diffraction (XRD) measurements were taken at ALBA Synchrotron (Cerdanyola del Vallès, Barcelona, Spain) at the BL04-MSPD by using a curved primary beam monochromator at a wavelength of 1.5406 Å (Copper radiation), recorded between 5 and 90° with a step width of 0.02°/S.

2.3 Manufacture of ZIF-8 and DOX/Ce6@ZIF-8@PDA

An improved method was used to prepare ultra-small ZIF-8 nanoparticles (Xie et al., 2019b). In short, 2-MI was added into methanol with $Zn(NO_3)_2{\cdot}6H_2O$. After 30-minute mixing at 25°C, the product was centrifuged. After resulting from the mixture of DOX and $Zn(NO_3)_2{\cdot}6H_2O$, DOX/ZIF-8 was prepared in the similar method. The final product was collected by centrifugation. Then, a ZIF-8 shell layer loaded with PS-Ce6 was uniformly grown around DOX/ZIF-8. Ce6 (6 mg) and DOX/ZIF-8 (60 mg) were first mixed in 2-MI solution and added to $Zn(NO_3)_2{\cdot}6H_2O$ solution in a ratio of 1:1. The mixing was continued for another 2 h at room temperature. The product was obtained by centrifugation, followed by the re-dissolution in ethanol. PDA (15 mg) was dispersed in 1 ml of ethanol and mixed with DZC solution (3 ml) for 2 h. Finally, the product was obtained by centrifugation.

2.4 Drug Release Detection

An ultraviolet spectrophotometer was used to analyze the released Ce6–visible spectrophotometer. DZCP was dissolved in PBS solution with a pH of 5.6, 6.5, or 7.4. The supernatant was collected at a predetermined time point and diluted in ethanol. According to the standard curve of free Ce6, the absorbance of Ce6 was read at 410 nm. In the DOX release study, DZCP was dissolved in PBS solution with pH 6.5 and 7.4. Both drug release detections were quantitatively analyzed.

2.5 ROS Generation

The DPBF probe was used to measure the singlet oxygen ($^1O_2$) produced by Ce6 under ultrasound. The DPBF solution, with pH 6.5 or 7.3, was inserted into DZCP, respectively. Next, the UV-DPBF analysis was carried out using a visible spectrophotometer, and extracellular hydroxyl radicals (•OH) produced were measured. After that, the resultant was added to PBS buffer, pH 6.5, containing MB and mixed well. For the ESR measurement, 100 μL of the sample aqueous solution (1 mg/L) was mixed with 500 μL of the TEMP solution. In addition to the use of DMPO (50 mM) as a spin capture agent, the •OH detection was also carried out in accordance with the aforementioned method.

2.6 Intracellular Hypoxia and ROS Detection

With DMEM (2 ml), 4T1 cells were seeded at 1×10^5 cells per well into a 12-well culture plate and incubated overnight at 37°C. The cells were incubated under normoxic conditions (21% oxygen) with 5% CO_2 or under an oxygen-deficient environment (1% oxygen) for 8 h. After 4 h of incubation with DZCP at 50 μg ml^{-1}, the ultrasound-treated group was subjected to ultrasonic waves at 1 MHz for 10 min, 1.5 W cm^{-2}. Then, the cyto-ID hypoxia/

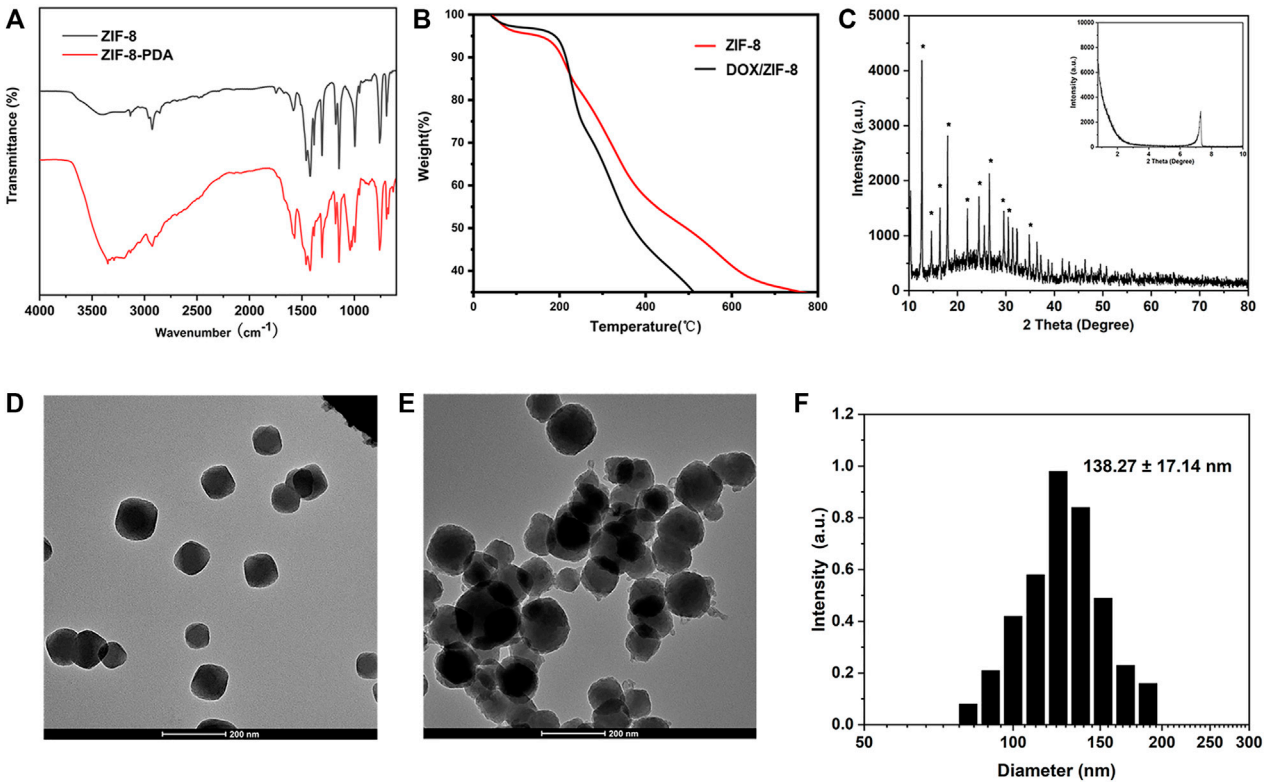

FIGURE 1 | (A) FT-IR spectra of ZIF-8 and ZIF-8/PDA. **(B)** TGA curves of ZIF-8 and DOX/ZIF-8. **(C)** XRD characterization of ZIF-8. The main peaks are labeled with stars. **(D,E)** DOX/ZIF-8 and DOX/Ce6@ZIF-8@PDATEM images. **(F)** DZCP diameter distribution in PBS.

oxidative stress detection kit was used, followed by fluorescent imaging. After washing several times with DI water, the cells were stained with DAPI.

2.7 Cell Viability Assay

The MTT method was applied to detect cytotoxicity. L929 and 4T1 cells were seeded in a 96-well plate at a rate of 1×10^4 cells each well and incubated under normoxia (21% oxygen) or hypoxia (1% oxygen) and 5% CO_2 condition for 8 h. Different doses of DZCP were applied to each well. The cells were incubated for another 20 h following the DZCP treatment before applying the MTT reagent. At 490 nm, the absorbance was recorded on the Bio-Rad 680 microplate reader.

2.8 *In Vivo* Experiments

Balb/c mice were purchased from the Experimental Animal Center of Shanghai Jiaotong University (Shanghai, China). Animal experiments were carried out in accordance with the standards of "China National Regulations on the Care and Use of Laboratory Animals." The mice with about 20 g weight were injected with 1×10^6 4T1 cells by hypodermic injection to establish a tumor-bearing model, which were then divided into three groups (PBS, DOX/Ce6@ZIF-8@PDA (DZCP), and DOX/Ce6@ZIF-8@PDA treatment group with ultrasound ($DZCP^+$)). For the *in vivo* experiment, the ultrasonic parameter was set as 1.0 MHz, 50% duty cycle, and 1.0 W cm^{-2}. All materials used Ce6 at a concentration of 4.0 mg kg^{-1} body weight. The nanoparticle IVs were operated on 1 and 3 days. After 24 h of injection, ultrasound was used during the treatment. Both body weight and tumor size were measured every 2 days. After 15 days, the mice were euthanized, and blood was collected for hematology research.

2.9 DZCP Biodistribution *In Vivo*

To evaluate DZCP biodistribution, after the injection, the *in vivo* fluorescence of mice was obtained at fixed intervals. In addition, the signal intensity of the nanoparticles was measured at the same time point to point out the metabolism of nanoparticles *in vivo*.

2.10 DZCP Signal Intensity *In Vivo*

To investigate the nanoparticle signal intensity *in vivo*, nude mice were divided into three groups and were intravenously injected with 100 μL of PBS, DZCP nanoparticles, and DZCP nanoparticles with SDT. Then, the T1-weighted images were acquired by *in vivo* imaging with a special animal imaging coil at room temperature. The T1-weighted signal intensities were acquired through *in vivo* imaging via manually drawn regions of interest.

2.11 Statistical Analysis

Data were statistically analyzed by OriginLab (OriginLab Corporation, Northampton, MA) and GraphPad Prism 7

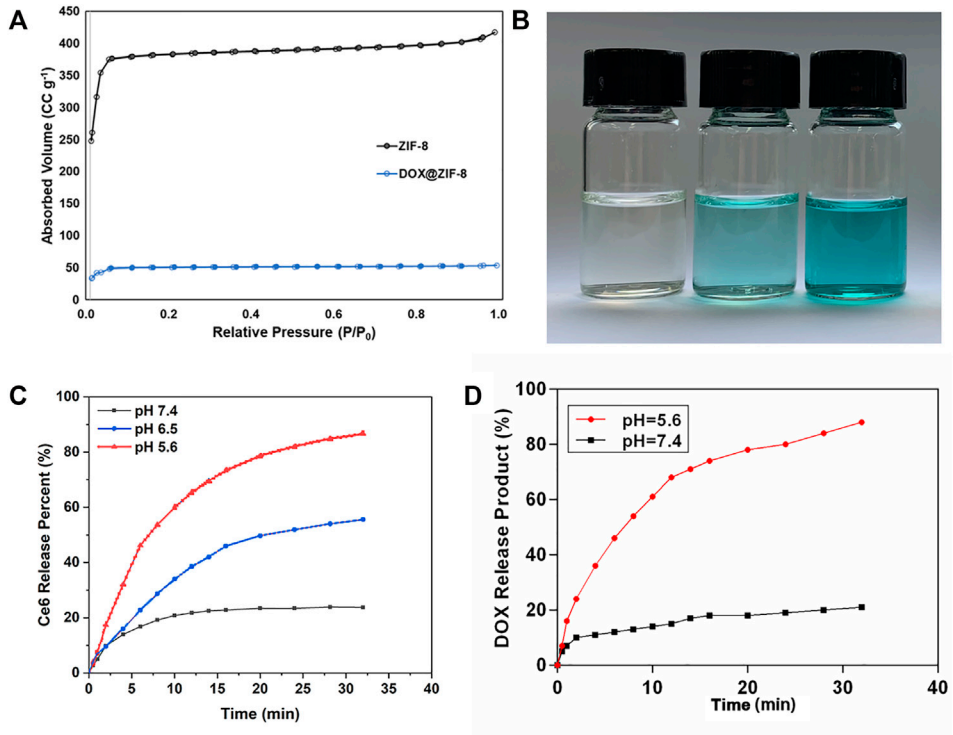

FIGURE 2 | (A) N_2 adsorption isotherms of ZIF-8 and DOX/ZIF-8. **(B)** Photos of ultrasound-treated DZCP solution. **(C)** Ce6-released behavior of DZCP in PBS solutions for different time points. **(D)** DOX-released behavior of DZCP after soaking in PBS solutions for different time points

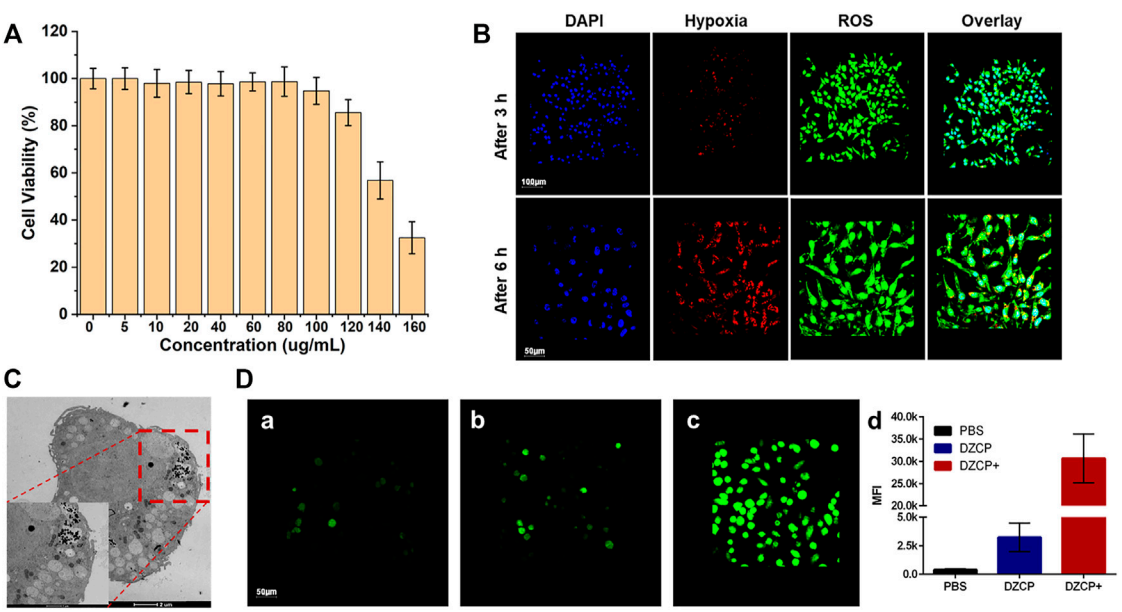

FIGURE 3 | (A) Relative viabilities of 4T1 cells treated with DZCP in the absence of ultrasonic waves for 24 h **(B)** ROS and hypoxia *in vitro* imaging of 4T1 cells. **(C)** TEM images of 4T1 cells after incubation with 160 μg/ml DZCP after 24 h. **(D)** Green fluorescence cell staining for ROS generation by 4T1 cells after treated with PBS, DZCP, or $DZCP^+$ under hypoxic conditions. The corresponding MFI values were analyzed and presented in (d). Green signals indicate the ROS generation.

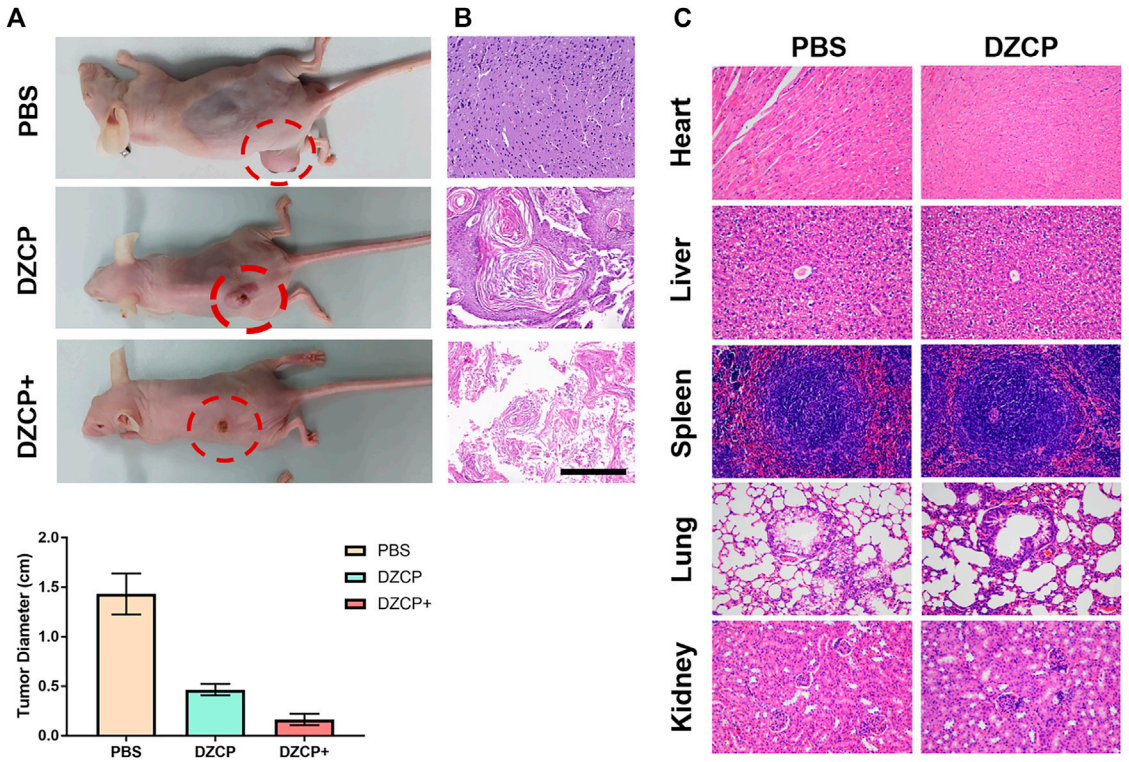

FIGURE 4 | (A) Photos of 4T1 tumor-bearing mice at the end of treatments. Comparison of the PBS, DZCP, and DZCP groups. Histological images of **(B)** tumor sections and **(C)** different tissue sections after treatment. Scale bar is 50 μm.

software (GraphPad Software, Inc., La Jolla, CA, United States). The *t*-test and one-way analysis of variance (ANOVA) were applied for significance analysis, followed by the Bonferroni test. $p < 0.05$ was considered to indicate a statistically significant difference. The open-source image analysis platform, ImageJ, was used in image acquisition and subsequent analysis.

3 RESULTS

3.1 Manufacture of DOX/Ce6@ZIF-8@PDA Nanocomposites

DOX/ZIF-8 crystals doped with DOX were constructed via an ion doping technology from previous reports. In the FT-IR result shown in **Figure 1**, at 1,584 cm^{-1}, an absorption peak of C=N stretching vibrations in ZIF-8 (**Figure 1A**) was obtained (Tran et al., 2020). The DOX loading detection was shown by TGA, suggesting a sharp weight loss in DOX/ZIF-8 compared to ZIF-8 between 300 and 450°C, which was due to the DOX decomposition (**Figure 1B**). Additionally, to characterize the ZIF-8 with its MOF structure, the X-ray diffraction (XRD) results are shown in **Figure 1C**. The small-angled XRD in the right corner of **Figure 1C** clearly verified the MOF architecture. The images of TEM demonstrated the size of DOX/ZIF-8 to be about 78 nm (**Figure 1D**). It also implied that Ce6 was loaded into the ZIF-8 shell by the one-pot process at the beginning. Finally, a polymer PDA was coated onto the DZC particles to improve their biocompatibility. In this case, the TEM image, **Figure 1E**, showed that DOX/Ce6@ZIF-8@PDA with an average size of about 135 nm was obtained. The DLS was also applied to DZCP to evaluate the diameter distribution in **Figure 1F** and presented 138.27 ± 17.14 nm of NP diameter, which was consistent with the TEM result.

3.2 pH-Responsive Drug Release Behavior

In this experiment, type I isotherms of DOX/ZIF-8 and ZIF-8 were shown by nitrogen adsorption/desorption experiments and proved the evidence of micropore presence (**Figure 2A**). Thus, the high amount of Ce6 and DOX loading and releasing could be expected in our study. To evaluate the degradability of DZCP with ultrasonic waves, nanoparticles were dispersed in PBS buffer of pH 7.4 and treated with ultrasound for 0, 5, and 10 min, respectively, as shown in **Figure 2B**. The ultrasonic parameter was set as 1.0 MHz and 1.5 W cm^{-2}. The complete destruction of DZCP could be shown by the different shades, confirming the sonodynamic sensitiveness of DZCP. Furthermore, the released Ce6 was detected via UV−Vis spectroscopy. With a decrease in pH to 5.6, almost 90% of Ce6 is released due to the decomposition of DZCP, as shown in **Figure 2C**. Thus, the result demonstrated that the drug release is negatively related to the pH value. A similar result was obtained in the *in vitro* experiment of DOX@ZIF-8 release behavior. In **Figure 2D**, the DOX release behaviors are studied under different conditions. At pH 7.4, the DOX@ZIF-

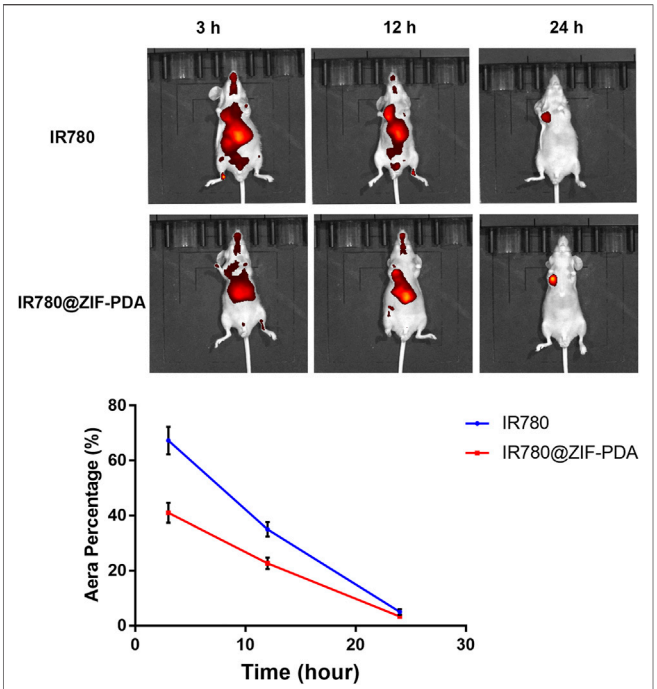

FIGURE 5 | *In vivo* imaging mice at 3, 12, and 24 h after tail vein injection of IR780 and IR780/ZIF-PDA, respectively.

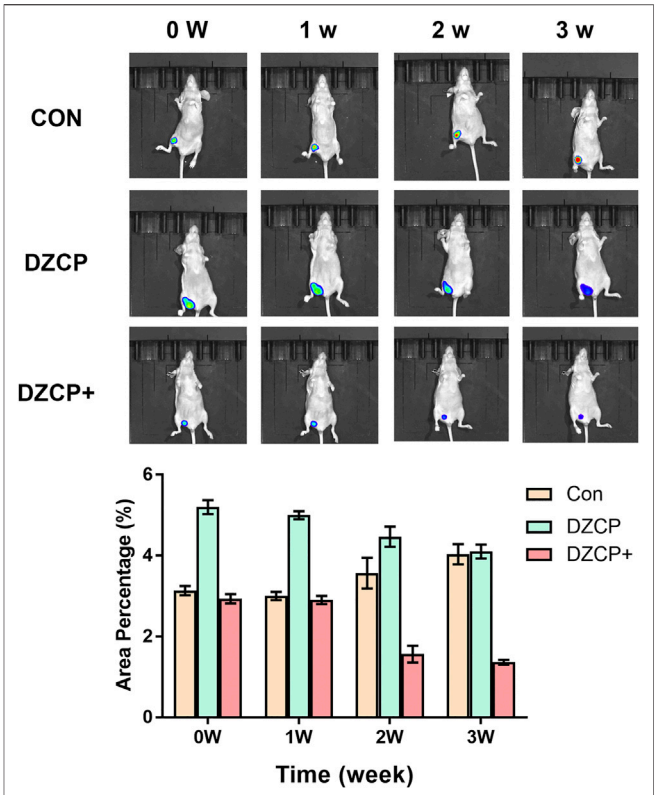

FIGURE 6 | *In vivo* imaging of mice at 0, 1, 2, and 3 weeks after tail vein injection of PBS, DZCP nanoparticles, and DZCP nanoparticles with SDT, respectively.

8 proved a poor drug leakage because of its immobilization into the framework of ZIF-8 at 48 h. After pH decreased to 5.6, nanoparticles collapsed and released DOX particles. Finally, about 88% of DOX is released into the aqueous environment under acidic conditions.

3.3 Cell Apoptosis Analysis

For the cytotoxicity test, MTT assay was used to evaluate the biocompatibility of DZCP to L929 cells. As shown in **Figure 3A**, at a concentration of 200 μg ml^{-1}, the cells treated with DZCP still showed a high survival rate, indicating the biological stability of DZCP. Due to its good biocompatibility, DZCP was gradually endocytosed by 4T1 cells within 6 h. At a concentration of 160 μg/ml, DZCP showed significantly increased cytotoxicity, indicating the importance of hypoxia alleviation for combination treatment.

3.4 Intracellular ROS and Hypoxia Detection

In order to measure the production of ROS, 4T1 cells were cultured *in vitro* and incubated with $DZCP^+$ (DZCP combined with ultrasonic treatment) under hypoxia (1% oxygen) conditions for 3 and 6 h, respectively. The ROS/hypoxia detection kit was used (**Figure 3B**), the characteristics of which are the same as the reported method (Silva et al., 2021; Zhang et al., 2021). The generated ROS was detected in $DZCP^+$-treated cells with the appearance of green fluorescence, demonstrating that ROS generation and tumor cells decrease under hypoxic conditions. This phenomenon was due to the enhanced ROS generation of nanoparticles in the SDT with time. Another TEM result shown in **Figure 3C** demonstrated the permeability and retention of DZCP in the 4T1 cells. After incubation with 160 μg/ml DZCP for 24 h, the 4T1 cells were sliced to exhibit the permeability of the nanoparticles. Benefited from the PDA layer, the amount of DZCP was promoted by enhanced endocytosis of the 4T1 cells. Most importantly, as shown in **Figure 3D**, the ROS production was additionally revealed by the fluorescence staining with the 4T1 cells, which were incubated with PBS, DZCP, and $DZCP^+$, respectively. Compared with PBS- or DZCP-treated cells in **Figures 3Da,b**, an increased appearance of green fluorescence was observed in $DZCP^+$-treated cells (shown in **Figure 3Dc**), demonstrating the success of ROS generation. In addition, the mean fluorescence intensity (MFI) results showed that the $DZCP^+$ group had significantly increased fluorescence intensity than the other two groups, which was about 8-fold of that in the PBS group.

3.5 *In Vivo* Tumor Inhibition

Balb/c mice with 4T1 tumor bearing were used to evaluate antitumor experiments *in vivo*. The experimental mice were randomly divided to receive PBS, DZCP, or $DZCP^+$ treatments. By the IVs, the mice were treated with the drugs with a Ce6 concentration of 4.0 mg kg^{-1}. Then, the $DZCP^+$ group was exposed to an ultrasound of 1 MHz for 10 min^{-2}. Fifteen days after the drug treatment, each group was monitored for body weight and tumor size. As shown in **Figure 4A**, in the mice treated with DZCP, the slight inhibition of tumor growth

indicated the improved effect of DOX released by DZCP. After ultrasonic treatment, the tumor-inhibiting ability of DZCP was significantly enhanced. On day 15, in the DZCP-treated group, the mice had about a one-third-size tumor of the DZCP group, suggesting the synergistic effect of SDT and DOX highly attributed to the antitumor effect. The H&E staining from the tumor of the three groups also reported tumor suppression, declaring that the tumors in the DZCP group showed more necrotic sections (**Figure 4B**). Additionally, histological analyses of mice in the PBS group and the DZCP group showed normal and similar cell shapes and tissue formation, which indicated that the side effect of DZCP was negligible and did not influence body health (**Figure 4C**). Also, almost no nanoparticles were detected on the slices, indicating that the DZCP was metabolized *in vivo* safely and there was no accumulation in the recipient mice. Those slices were obtained from important organs in the body, including the heart, liver, spleen, lung, and kidney.

3.6 DZCP Biodistribution *In Vivo*

To evaluate the DZCP biodistribution *in vivo*, the images of small animals were screened to the mice at intervals by IVs. The zinc levels were determined by the signal intensities. The quantitative analysis in **Figure 5** clearly shows a decreased trend of the DZCP with time. It suggested that DZCP accumulated in the liver and moved to the spleen at the first 12 h after injection. From 12 h, the biodistribution result suggested that the DZCP accumulation amount began to reduce by the incremental time.

3.7 *In Vivo* Signal Intensity of DZCP

As the benefit of the five mismatched electrons of Zn^{2+}, one of the possible applications of ZIF-8 nanoparticles is the effective contrast agents in *in vivo* imaging. Thus, after the IVs of DZCP nanoparticles into the tumor-bearing mice, it was obvious that T1-weighted MR signals could be clearly observed with enhancement at the tumor site compared with the PBS group. The results revealed that the DZCP group signal intensity after intravenous injection for 3 weeks showed a slight decrease, suggesting that a cumulative accumulation process of DZCP in the mice could last a long period of time (**Figure 6**). Due to the EPR effect, the time point of the maximum cumulative amount of DZCP in tumors is about 24 h (shown in **Figure 6**). In addition, with SDT treatment, the signal intensity of DZCP decreased from 2 weeks, demonstrating the faster metabolism of DZCP with SDT. Comparing to the PBS-treated group, the signal intensity of DZCP with SDT was similar after 2 weeks. Therefore, due to the complexity of an *in vivo* microenvironment, the DZCP nanoparticles with SDT were able to gradually collapse into small ions and molecules, followed by the movement of mice metabolic systems in a relatively rapid manner.

4 DISCUSSION

Aiming at creating an effective nanoplatform for tumor therapy, we concentrated on the delivery and the tumor inhibition capacities of the nanocomposites and synthesized an SDT-controlled nanoparticle. With the characterization results of this synthesized nanoparticle, it is clear that a crystal with a DOX/ZIF-8 composite structure was created, as indicated by the FT-IR and TGA in **Figures 1A,B**. The detection of the DOX with a high weight loss percentage during the TGA process in this MOF crystal demonstrated that the structure created in the experiment can be a carrier for a high amount of drug delivery. Thus, it could be used for a drug combination treatment in tumor therapy, DOX, and Ce6. In addition, during tumor therapy, there was a positive relation between the endocytosis efficiency of the nanoparticle and its tumor inhibition capacity, which requested a suitable nanoparticle size for the carrier cage. It is reported that 100-nm-size nanoparticles could be transported into the blood vessels in a tumor microenvironment via the EPR effect. Therefore, as shown in **Figure 1D**, our nanocomposite with an average diameter size of 100 nm will be effective for the endocytosis of tumor cells. Moreover, the PDA layer coated around DZC could improve the biocompatibility of nanocomposites and decrease the leak of the drug content during delivery.

From the nanoparticle structure results, a high amount of Ce6 and DOX loading and releasing can be expected in our study. It was confirmed by the *in vitro* release behavior, investigated in **Figure 2**. According to the special pH microenvironment of the tumor, the DOX and Ce6 release behaviors were studied under different conditions, as described in **Section 3.2** in **Figure 2**. Compared to the poor drug leakage results of DOX and Ce6 at pH 7.4, both DOX and Ce6 molecules were quickly released into the aqueous environment under acidic conditions, which were up to more than 80%. This phenomenon was because the framework of the nanoparticles collapsed at pH 5.6. The aforementioned results suggest that DZCP has great potential to be used as an effective drug delivery system for tumor tissues under acidic conditions (Zhang et al., 2020).

As described in a previous study, a single treatment to tumor cells is less efficient and suggests that synergetic therapy needs to be studied. In this research, significantly enhanced cytotoxicity to the tumor cell, L929 cells, was found, which was due to the high drug content in DZCP nanoparticles and their hypoxia alleviation in synergetic therapy. As described in **Section 3.4**, the generated ROS in $DZCP^{+}$-treated cells decreased tumor cells by damaging hypoxic conditions. As shown in **Figure 3**, the improved ROS generation capability of DZCP with SDT treatment group could destroy tumor hypoxia successfully, with its construction damaged the generation of the great quantity of ROS could be facilitated in living tumor cells. Most importantly, as shown in **Figure 3D**, the comparison of the amount of ROS generated between the PBS, DZCP, and $DZCP^{+}$-treated groups demonstrated that abundant O_2 released from DZCP was controlled by the ultrasonic waves in the acidic TME. The intracellular detection results suggest that the DZCP nanocomposites could be used for efficient tumor hypoxia alleviation and *in vitro* tumor therapy, which prevented the drug leakage and premature failure before its arrival into the tumor microenvironment (Kang et al., 2020).

As suggested by *in vitro* experiment results, our DZCP nanoparticles could be an effective tumor therapy. Therefore,

in vivo experiments were used to further characterize their treatment efficiency in the cancer cells. According to the tumor suppression behavior in **Figure 4**, necrosis slices and eliminations of tumor tissues of the $DZCP^{+}$- treated mice group confirmed the capacity of tumor inhibition of the nanocomposite. More histological results in organs demonstrated the negligible side effects of DZCP. Those slices indicated the safety of the nanocomposite and implied the possibility of its clinical use in the future. In summary, the DZCP with SDT could be used as an efficient and biocompatible nanodrug for enhanced synergistic therapy.

Moreover, the long-term toxicity of nanoparticles was also concentrated by researchers, which was requested to be minimized by clinical requirements. From the results shown in **Figures 5**, **6**, the DZCP distribution and decomposition behaviors were determined. The results described in **Sections 3.5**, **3.6** implied that nanoparticles could accumulate into tumor tissues, instead of the organs, and gradually decompose into small molecules and ions after a period of time. Compared to other inorganic solid nanoparticles for which such effective body removal is difficult to achieve, the decomposition behavior of DZCP might a preferable selection. Hence, the *in vivo* experiments suggested the DZCP with SDT can be a suitable option for tumor therapy in the future.

5 CONCLUSION

In conclusion, we successfully established a core–shell-structured nanoplatform, DOX/Ce6@ZIF-8@PDA(DZCP), with TME responses for combination sonodynamic/DOX therapy. Under ultrasonic waves, the doped DOX could inhibit cancer cells, which could also cooperate with Ce6, in favor of overcoming hypoxic TME conditions and generate ROS products. Moreover, with ultrasound-controlled ROS release, the antitumor efficacy was highly improved. Thus, both *in vitro* and *in vivo* experiments demonstrate an improved antitumor efficacy for DZCP by O_2 and DOX replenishment in the clinical synergistic treatment. These integrated nanocomposites may draw attention and inspire novel ideas for preparing highly efficient treatment reagents for clinical tumor therapy (Tao et al., 2021).

DATA AVAILABILITY STATEMENT

The original contributions presented in the study are included in the article/Supplementary Material, further inquiries can be directed to the corresponding author.

ETHICS STATEMENT

The animal study was reviewed and approved by Center of Experimental Animals, Shanghai Jiaotong University.

AUTHOR CONTRIBUTIONS

LZ took part in writing—original draft, investigation, and methodology; TY helped frame the methodology; PL assisted with methodology and supervision; LS took part in methodology; JL helped with methodology; and LG involved in supervision, writing—original draft and writing—review and editing.

FUNDING

This research was funded by the Science and technology development fund of Pudong New Area (PKJ 2020-09) and the Inter-disciplinary Program of Shanghai Jiao Tong University (YG2017QN40).

REFERENCES

Adhikari, C., Das, A., and Chakraborty, A. (2015). Zeolitic Imidazole Framework (ZIF) Nanospheres for Easy Encapsulation and Controlled Release of an Anticancer Drug Doxorubicin under Different External Stimuli: A Way toward Smart Drug Delivery System. *Mol. Pharmaceutics* 12 (9), 3158–3166. doi:10.1021/acs.molpharmaceut.5b00043

Banerjee, R., Phan, A., Wang, B., Knobler, C., Furukawa, H., O'Keeffe, M., et al. (2008). High-Throughput Synthesis of Zeolitic Imidazolate Frameworks and Application to CO 2 Capture. *Science* 319 (5865), 939–943. doi:10.1126/science.1152516

Basaleh, A. S., and Sheta, S. M. (2021). Manganese Metal-Organic Framework: Chemical Stability, Photoluminescence Studies, and Biosensing Application. *J. Inorg. Organomet. Polym.* 31 (4), 1726–1737. doi:10.1007/s10904-021-01888-4

Cabral, H., Miyata, K., Osada, K., and Kataoka, K. (2018). Block Copolymer Micelles in Nanomedicine Applications. *Chem. Rev.* 118 (14), 6844–6892. doi:10.1021/acs.chemrev.8b00199

Cai, X., Xie, Z., Ding, B., Shao, S., Liang, S., Pang, M., et al. (2019). Monodispersed Copper(I)-Based Nano Metal-Organic Framework as a Biodegradable Drug Carrier with Enhanced Photodynamic Therapy Efficacy. *Adv. Sci.* 6 (15), 1900848. doi:10.1002/advs.201900848

Cheng, Y., Cheng, H., Jiang, C., Qiu, X., Wang, K., Huan, W., et al. (2015). Perfluorocarbon Nanoparticles Enhance Reactive Oxygen Levels and Tumour Growth Inhibition in Photodynamic Therapy. *Nat. Commun.* 6, 8785. doi:10.1038/ncomms9785

Choi, Y. J., Lee, J., Ha, S. H., Lee, H. K., Lim, H. M., Yu, S. H., et al. (2021). 6, 8-Diprenylorobol Induces Apoptosis in Human colon Cancer Cells via Activation of Intracellular Reactive Oxygen Species and P53. *Environ. Toxicol.* 36 (5), 914–925. doi:10.1002/tox.23093

Fan, W., Huang, P., and Chen, X. (2016). Overcoming the Achilles' Heel of Photodynamic Therapy. *Chem. Soc. Rev.* 45 (23), 6488–6519. doi:10.1039/c6cs00616g

Frésard, L., Smail, C., Smail, C., Ferraro, N. M., Teran, N. A., Li, X., et al. (2019). Identification of Rare-Disease Genes Using Blood Transcriptome Sequencing and Large Control Cohorts. *Nat. Med.* 25 (6), 911–919. doi:10.1038/s41591-019-0457-8

Guo, N., Zhou, Y., Wang, T., Lin, M., and Han, M. (2020). Specifically Eliminating Tumor-Associated Macrophages with an Extra- and Intracellular Stepwise-Responsive Nanocarrier for Inhibiting Metastasis. *ACS Appl. Mater. Inter.* 12 (52). doi:10.1021/acsami.0c19301

Ha, L., Choi, K. M., and Kim, D. P. (2021). Interwoven MOF-Coated Janus Cells as a Novel Carrier of Toxic Proteins. *ACS Appl. Mater. Inter.* 13:18545–18553. doi:10.1021/acsami.1c01927

Kang, Y., Yu, X., Fan, X., Aodenggerile Zhao, S., Tu, C., et al. (2020). Tetramodal Imaging and Synergistic Cancer Radio-Chemotherapy Enabled by Multiple Component-Encapsulated Zeolitic Imidazolate Frameworks. *ACS Nano* 14 (4), 4336–4351. doi:10.1021/acsnano.9b09858

Lan, G., Ni, K., and Lin, W. (2019). Nanoscale Metal-Organic Frameworks for Phototherapy of Cancer. *Coord. Chem. Rev.* 379, 65–81. doi:10.1016/j.ccr.2017.09.007

Li, J., Ge, Z., Toh, K., Liu, X., Dirisala, A., Ke, W., et al. (2021). Enzymatically Transformable Polymersome-Based Nanotherapeutics to Eliminate Minimal Relapsable Cancer. *Adv. Mater.* 33 (49), 2105254. doi:10.1002/adma.202105254

Li, J., and Kataoka, K. (2021). Chemo-physical Strategies to Advance the *In Vivo* Functionality of Targeted Nanomedicine: The Next Generation. *J. Am. Chem. Soc.* 143 (2), 538–559. doi:10.1021/jacs.0c09029

Li, J., Wei, K., Zuo, S., Xu, Y., Zha, Z., Ke, W., et al. (2017). Light-Triggered Clustered Vesicles with Self-Supplied Oxygen and Tissue Penetrability for Photodynamic Therapy against Hypoxic Tumor. *Adv. Funct. Mater.* 27 (33), 1702108. doi:10.1002/adfm.201702108

Liédana, N., Galve, A., Rubio, C., Téllez, C., and Coronas, J. (2012). CAF@ZIF-8: One-step Encapsulation of Caffeine in MOF. *ACS Appl. Mater. Inter.* 4 (9), 5016–5021. doi:10.1021/am301365h

Lu, Z., Knobler, C. B., Furukawa, H., Wang, B., Liu, G., and Yaghi, O. M. (2009). Synthesis and Structure of Chemically Stable Metal–Organic Polyhedra. *J. Am. Chem. Soc.* 131 (35), 12532–12533. doi:10.1021/ja905101s

Modery-Pawlowski, C. L., Tian, L. L., Pan, V., and Sen Gupta, A. (2013). Synthetic Approaches to RBC Mimicry and Oxygen Carrier Systems. *Biomacromolecules* 14 (4), 939–948. doi:10.1021/bm400074t

Ng, J. Y., Obuobi, S., Chua, M. L., Zhang, C., Hong, S., Kumar, Y., et al. (2020). Biomimicry of Microbial Polysaccharide Hydrogels for Tissue Engineering and Regenerative Medicine - A Review. *Carbohydr. Polym.* 241, 116345. doi:10.1016/j.carbpol.2020.116345

Park, K. S., Ni, Z., Cote, A. P., Choi, J. Y., Huang, R., Uribe-Romo, F. J., et al. (2006). Exceptional Chemical and thermal Stability of Zeolitic Imidazolate Frameworks. *Proc. Natl. Acad. Sci.* 103 (27), 10186–10191. doi:10.1073/pnas.0602439103

Poinard, B., Neo, S. Z. Y., Yeo, E. L. L., Heng, H. P. S., Neoh, K. G., and Kah, J. C. Y. (2018). Polydopamine Nanoparticles Enhance Drug Release for Combined Photodynamic and Photothermal Therapy. *ACS Appl. Mater. Inter.* 10 (25), 21125–21136. doi:10.1021/acsami.8b04799

Pouysségur, J., Dayan, F., and Mazure, N. M. (2006). Hypoxia Signalling in Cancer and Approaches to Enforce Tumour Regression. *Nature* 441 (7092), 437–443. doi:10.1038/nature04871

Sharma, P., and Allison, J. P. (2015). Immune Checkpoint Targeting in Cancer Therapy: toward Combination Strategies with Curative Potential. *Cell* 161 (2), 205–214. doi:10.1016/j.cell.2015.03.030

Sheta, S. M., El-Sheikh, S. M., Abd-Elzaher, M. M., Ghanem, M. L., and Salem, S. R. (2019). A Novel, Fast, High Sensitivity Biosensor for Supporting Therapeutic Decisions and Onset Actions for Chest Pain Cases. *RSC Adv.* 9 (35), 20463–20471. doi:10.1039/c9ra03030a

Shi, J., Kantoff, P. W., Wooster, R., and Farokhzad, O. C. (2017). Cancer Nanomedicine: Progress, Challenges and Opportunities. *Nat. Rev. Cancer* 17 (1), 20–37. doi:10.1038/nrc.2016.108

Siegel, R. L., Miller, K. D., and Jemal, A. (2017). Cancer Statistics, 2017. *CA: A Cancer J. Clinicians* 67 (1), 7–30. doi:10.3322/caac.21387

Silva, A., Carvalho, N. V., Paterno, L. G., Moura, L. D., Filomeno, C. L., Paula, E. D., et al. (2021). Methylene Blue Associated with Maghemite Nanoparticles Has Antitumor Activity in Breast and Ovarian Carcinoma Cell Lines. *Cancer Nanotechnology* 12 (1), 1–21. doi:10.1186/s12645-021-00083-x

Sun, L., Ma, Y., Niu, H., Liu, Y., Yuan, Y., and Liu, C. (2021). Recapitulation of *In Situ* Endochondral Ossification Using an Injectable Hypoxia-Mimetic Hydrogel. *Adv. Funct. Mater.* 31 (5), 2008515. doi:10.1002/adfm.202008515

Tao, Y., Sun, Y., Shi, K., Pei, P., Ge, F., Yang, K., et al. (2021). Versatile Labeling of Multiple Radionuclides onto a Nanoscale Metal–Organic Framework for Tumor Imaging and Radioisotope Therapy. *Biomater. Sci.* 9, 2947–2954. doi:10.1039/d0bm02225j

Tran, H. T. N., Ang, K. S., Chevrier, M., Zhang, X., Lee, N. Y. S., Goh, M., et al. (2020). A Benchmark of Batch-Effect Correction Methods for Single-Cell RNA Sequencing Data. *Genome Biol.* 21 (1), 12. doi:10.1186/s13059-019-1850-9

Wang, B., Côté, A. P., Furukawa, H., O'Keeffe, M., and Yaghi, O. M. (2008). Colossal Cages in Zeolitic Imidazolate Frameworks as Selective Carbon Dioxide Reservoirs. *Nature* 453 (7192), 207–211. doi:10.1038/nature06900

Xie, Z., Cai, X., Sun, C., Liang, S., Shao, S., Huang, S., et al. (2019a). O2-Loaded pH-Responsive Multifunctional Nanodrug Carrier for Overcoming Hypoxia and Highly Efficient Chemo-Photodynamic Cancer Therapy. *Chem. Mater.* 31 (2), 483–490. doi:10.1021/acs.chemmater.8b04321

Xie, Z., Liang, S., Cai, X., Ding, B., Huang, S., Hou, Z., et al. (2019b). O2-Cu/ZIF-8@Ce6/ZIF-8@F127 Composite as a Tumor Microenvironment-Responsive Nanoplatform with Enhanced Photo-/Chemodynamic Antitumor Efficacy. *ACS Appl. Mater. Inter.* 11 (35), 31671–31680. doi:10.1021/acsami.9b10685

Zeng, R., He, T., Lu, L., Li, K., Luo, Z., and Cai, K. (2021). Ultra-thin Metal-Organic Framework Nanosheets for Chemo-Photodynamic Synergistic Therapy. *J. Mater. Chem. B* 9 (20), 4143–4153. doi:10.1039/d1tb00528f

Zhang, C., Liu, Z., Zhang, Y., Ma, L., Song, E., and Song, Y. (2020). "Iron Free" Zinc Oxide Nanoparticles with Ion-Leaking Properties Disrupt Intracellular ROS and Iron Homeostasis to Induce Ferroptosis. *Cell Death Dis* 11 (3), 183. doi:10.1038/s41419-020-2384-5

Zhang, K., Zhou, X., Wang, J., Zhou, Y., Qi, W., Chen, H., et al. (2021). Dendrobium Officinale Polysaccharide Triggers Mitochondrial Disorder to Induce colon Cancer Cell Death via ROS-AMPK-Autophagy Pathway. *Carbohydr. Polym.* 264 (2), 118018. doi:10.1016/j.carbpol.2021.118018

Zhao, D., Shui, J.-L., Chen, C., Chen, X., Reprogle, B. M., Wang, D., et al. (2012). Iron Imidazolate Framework as Precursor for Electrocatalysts in Polymer Electrolyte Membrane Fuel Cells. *Chem. Sci.* 3 (11), 3200–3205. doi:10.1039/C2SC20657A

Zhou, Z., Song, J., Nie, L., and Chen, X. (2016). Reactive Oxygen Species Generating Systems Meeting Challenges of Photodynamic Cancer Therapy. *Chem. Soc. Rev.* 45 (23), 6597–6626. doi:10.1039/c6cs00271d

Conflict of Interest: The authors declare that the research was conducted in the absence of any commercial or financial relationships that could be construed as a potential conflict of interest.

Publisher's Note: All claims expressed in this article are solely those of the authors and do not necessarily represent those of their affiliated organizations, or those of the publisher, the editors, and the reviewers. Any product that may be evaluated in this article, or claim that may be made by its manufacturer, is not guaranteed or endorsed by the publisher.